

# SIMULATING CMS CALORIMETER RESPONSE OF ELECTROMAGNETIC SHOWERS USING MONTE CARLO METHODS

DEVAL DELIWALA<sup>1</sup>

<sup>1</sup> *University of California, Berkeley*

## ABSTRACT

Accurate simulation of electromagnetic shower development within the Compact Muon Solenoid (CMS) electromagnetic calorimeter (ECAL) is essential for precise energy measurements in high-energy physics experiments. This study presents a Monte Carlo simulation that models the longitudinal development of electromagnetic showers using a one-dimensional approximation. Phase 1 focuses on simulating the shower profile for 1 GeV incident electrons in a 25 cm lead tungstate (PbWO<sub>4</sub>) calorimeter, validating the simulation against established benchmarks. Phase 2 assesses the detector's linearity and energy resolution by calibrating the energy deposition and examining its dependence on varying incident energies (1, 3, 5, and 10 GeV). Phase 3 involves fitting the energy deposition function to a gamma distribution, extracting parameters that characterize the shower development. Phase 4 explores the detector's performance as a function of calorimeter thickness, investigating the onset of non-linearities in energy response and the scaling of energy resolution. The simulation demonstrates a linear relationship between incident energy and mean energy deposited, as well as a square root scaling of energy resolution with energy, consistent with CMS expectations. These foundational phases establish a framework for further exploration into more complex shower dynamics and detector performance metrics.

## 1. INTRODUCTION

Accurate measurement of particle energies is fundamental to high energy physics experiments. Electromagnetic calorimeters (ECALs) are essential for detecting and measuring the energy of electrons and photons produced in particle collisions (e.g. [Group and Workman \(2022\)](#)). The CMS ECAL, constructed from lead tungstate (PbWO<sub>4</sub>) crystals, is designed to deliver high-resolution energy measurements crucial for a broad spectrum of physics analyses, including the identification of Higgs Boson decays and searches for new particles ([Brown 2007](#)).

Understanding the longitudinal development of electromagnetic showers within the ECAL is vital for optimizing its performance and interpreting experimental data. This study employs a Monte Carlo simulation with simplifying assumptions to model the longitudinal distribution of charged particles and photons generated by electromagnetic showers initiated by incident electrons. The work is divided into four primary phases:

1. *Phase 1*: Simulates the one-dimensional longitudinal development for 1 GeV incident electrons, validating the simulation against established benchmarks.

2. *Phase 2*: Assesses the detector's linearity and energy resolution across multiple incident energies (1, 3, 5, and 10 GeV).
3. *Phase 3*: Fits the energy deposition function to a gamma distribution, extracting parameters that characterize the shower development.
4. *Phase 4*: Examines the detector's performance as a function of calorimeter thickness, investigating the onset of non-linearities in energy response and analyzing the scaling of energy resolution.

The results provide insights into the functional dependence of shower development on energy and validate the simulation against established benchmarks.

This paper is structured as follows: Section 2 provides a detailed description of the CMS electromagnetic calorimeter. Section 3 outlines the simulation methods, including the assumptions and computational techniques used in Phases 1 through 4 of the project and presents the simulation results for each phase. Section 4 offers conclusions and discusses future work.

## 2. THE ELECTROMAGNETIC CALORIMETER

The CMS electromagnetic calorimeter is a critical component of the CMS detector at the Large Hadron

Collider (LHC). It is designed to measure the energy of electrons and photons with high precision and is composed of approximately 61,200 lead tungstate ( $\text{PbWO}_4$ ) crystals. These crystals are chosen for their high density, short radiation length, and fast “scintillation” properties, which are essential for the detection of high-energy particles within a compact volume.

Key features of the CMS ECAL include: (CMS Collaboration 2024)

1. *Material Composition*:  $\text{PbWO}_4$  crystals serve as the active medium, providing a dense material that facilitates the development of electromagnetic showers within a relatively short distance.
2. *Geometry and Depth*: The ECAL is segmented into a barrel region and two endcaps, each consisting of multiple layers of crystals. The total depth of the calorimeter is approximately 23 cm, corresponding to  $\sim 25$  radiation lengths, which is sufficient to contain the majority of electromagnetic showers initiated by high-energy electrons and photons.
3. *Readout System*: Each crystal is coupled to a photodetector, typically a photodiode or avalanche photodiode (APD), which converts the scintillation light into an electrical signal. The readout system is designed to handle high rates of particle interactions and provide precise energy measurements.
4. *Energy Resolution*: The ECAL achieves excellent energy resolution, which is critical for distinguishing between different particle types and for precise measurements of particle energies. The resolution depends on factors such as the number of crystals, the quality of the scintillation process, and the precision of the readout electronics.

Understanding the longitudinal development of electromagnetic showers within the ECAL is essential for optimizing its performance and ensuring accurate energy measurements. This study focuses on simulating this development using a simplified one-dimensional model, ignoring transverse spreading, laying the groundwork for more comprehensive simulations that account for three-dimensional shower characteristics and additional physical processes.

### 3. METHODS

This section outlines the Monte Carlo simulation approach used to model the one-dimensional longitudinal development of electromagnetic showers in the CMS ECAL.

#### 3.1. Phase 1: Monte Carlo Simulation of the Charged Particle and Photon Distribution

The objective of Phase 1 is to develop a Monte Carlo simulation that predicts the longitudinal development of an electromagnetic shower initiated by 1 GeV electrons in a 25 cm deep lead tungstate ( $\text{PbWO}_4$ ) calorimeter. The simulation aims to first generate a plot of the average number of charged particles (only considering positron-electron pairs, as will be discussed shortly) as a function of the distance from the incident face of the calorimeter. Afterwards the averaged number of photons generated via bremsstrahlung will additionally be plotted and compared against the number of electrons and positrons. The collective results for electron, positron, and photon counts as a function of calorimeter depth are compared to standardized values from the Particle Data Group (PDG) to assess simulation accuracy.

##### 3.1.1. Simplifying Assumptions

To make the simulation tractable, several simplifying assumptions are employed. These assumptions deviate from the real-world behavior of electromagnetic showers but allow for a foundational understanding of the shower development process.

1. *Calorimeter Geometry*: The ECAL is modeled as a uniform, one-dimensional crystal of  $\text{PbWO}_4$  with a depth of 25 cm. Electrons are assumed to enter the front face of the crystal with a fixed energy of 1 GeV and normal incidence.
2. *One-Dimensional Shower Development*: Real electromagnetic showers develop in three dimensions, exhibiting both longitudinal and transverse spread. For simplicity, the simulation employs a one-dimensional model, neglecting any transverse spreading of the shower.
3. *Discretized Bremsstrahlung*: Electrons lose energy primarily through bremsstrahlung. Instead of modeling this as a continuous process, the simulation approximates energy loss as discrete events occurring at random positions along the electron’s trajectory. The probability of a bremsstrahlung event occurring within a differential distance  $dx$  in the simulation is given by:

$$dP = \frac{dN}{N} = -\frac{dx}{X_0}.$$

where  $X_0$  is the radiation length of  $\text{PbWO}_4$  ( $\sim 0.89\text{cm}$ ).

4. **Equal Energy Division:** Upon a bremsstrahlung event, the energy is equally divided between the outgoing electron and the emitted photon. This is an unrealistic simplification, as the actual bremsstrahlung spectrum is peaked at low photon energies.
5. **Constant Ionization Energy Loss:** Charged particle's ( $e^+$  and  $e^-$ ) lose energy via ionization at a constant rate per centimeter penetrated. The energy loss  $dE/dx$  is taken from PDG's *Atomic and Nuclear Properties of Materials* online software and is  $\sim 11.5$  MeV lost per radiation length  $X_0$ . Therefore,

$$\frac{dE}{dx} \approx 12.92 \frac{\text{MeV}}{\text{cm}}.$$

The simulation also ignores the Landau distribution of energy loss and the Bragg peak effect as particles come to rest.

6. **Photon Interactions:** Photons interact primarily through electron-positron pair production in this simulation. The chosen probability of pair production within a differential distance  $dx$  is given by

$$dP = \frac{dx}{\frac{9}{7}X_0}.$$

Upon pair production, the resulting electron and positron share the photon's energy *equally*, and electrons are treated as massless particles.

### 3.1.2. Simulation Procedure

The simulation follows these steps for each event:

1. **Initialization:** Start with a single 1 GeV electron at the front face ( $x = 0$  cm) of the 25 cm  $\text{PbWO}_4$  calorimeter.
2. **Track Management:** Maintain a list of active particles (electrons, positrons, and photons) with their respective energies and positions.
3. **Energy Loss and Interactions:**
  - For each charged particle, determine the distance to the next bremsstrahlung event based on the radiation length  $X_0$ .
  - At each bremsstrahlung event, split the energy equally between the outgoing electron and the emitted photon.
  - For each photon, determine the distance to the possible next pair production event using the modified radiation length ( $\frac{9}{7}X_0$ ).
  - At each pair production event, generate an electron-positron pair, each receiving half of the photon's energy.
4. **Energy Loss via Ionization:** For each charged particle, subtract the ionization energy loss per centimeter from its energy as it traverses the calorimeter. If a particle's energy drops to zero or below, it is removed from the active list.
5. **Position Update:** Advance the position of each particle based on the distances traveled during interactions and energy loss.
6. **Event Termination:** Continue the simulation until all particles have either exited the calorimeter or been absorbed due to energy loss.

### 3.1.3. Data Collection and Analysis

Only the number of charged particles ( $e^+$  and  $e^-$ ) generated via photon pair production are first considered. For each simulated event, the positions where charged particles cross planes at specific depths from the front face of the calorimeter are recorded. After simulating 1000 events to reduce any statistical uncertainty, the average number of charged particles crossing each plane is computed. These averages are then plotted as functions of the calorimeter depth shown in Figure 1.

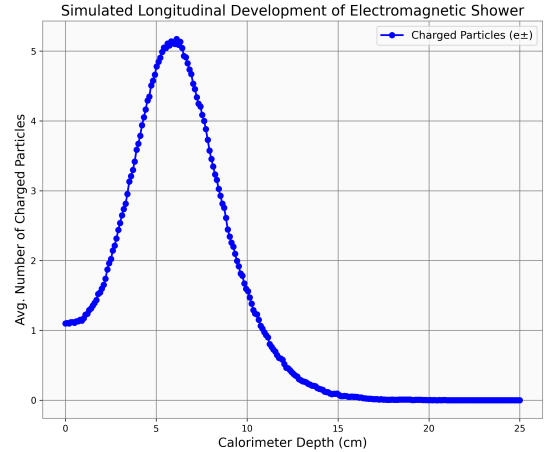


**Figure 1.** Average number of charged particles as a function of calorimeter depth for 1 GeV incident electrons. The distribution exhibits a peak at approximately 6.3 cm with around 9 charged particles crossing a plane at this depth. The shape closely resembles the charged particle distribution shown in PDG Passage of Particles Through Matter Figure 33.20.

The above plot shows a similar distribution to the established benchmarks such as Figure 33.20 in [Groom](#)

and Klein (2019), which showcases simulation results from an *iron* calorimeter using an EGS4 simulation (Agostinelli et al. 2003) of a 30 GeV electron-induced shower. The number of charged particles across the calorimeter follows a normal distribution with a peak of  $\sim 95$  charged particles at  $\sim 6$  radiation lengths in iron for a 30 GeV incident shower and a peak of around 9 charged particles at  $\sim 7.86$  radiation lengths in lead tungstate for a 1 GeV incident shower. This of course makes sense as increased incident energy gives rise to more chances of pair production occurring giving rise to more charged particles in the EGS4 simulation relative to the simplified one presented here.

To ensure the simulated simulation matches the EGS4 simulation PDG performed, the number of photons across the calorimeter is also considered. As shown in Figure 33.20 of Groom and Klein (2019), the photon distribution follows a similar pattern as the charged particle distribution but reaches a lower peak and at a later calorimeter depth and showcases more photons afterwards crossing deeper depths of the calorimeter than charged particles. Overplotting the photon distribution alongside the previously simulated charged particle distribution showcases similar results to the EGS4 simulation, with photon counts peaking at a deeper radiation length and surpassing the number of charged particles afterwards (see Figure 2). Of course, both distributions tend to 0 as the particles increasingly lose energy and get absorbed at higher depths.

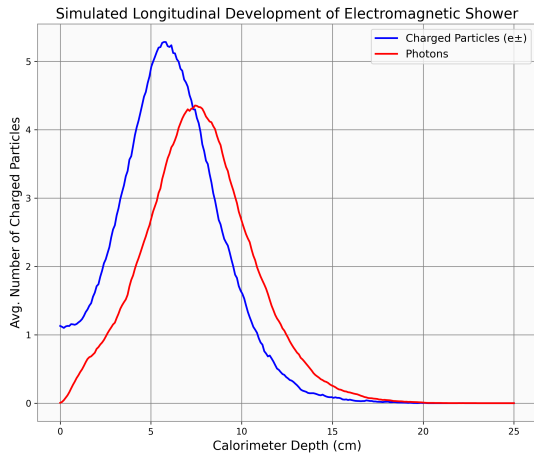


**Figure 2.** Comparison of average charged particle density and photon density as functions of calorimeter depth for 1 GeV incident electrons. The number of photons peaks after the charged particles, with the charged particle density only surpassing the photon density prior to its peak, in agreement with PDG’s EGS4 simulation results.

While the simulation described above employs a one-dimensional model uses a lead tungstate calorimeter instead of iron, the general features of the shower development, such as the position of the shower maximum and the relative densities of charged particles and photons, align qualitatively with the PDG benchmarks. Quantitative differences arise due to the simplifying assumptions and differences in material properties and incident energies.

### 3.2. Phase 2: Linearity and Energy Resolution of the Detector

Phase 2 extends the Monte Carlo simulation to evaluate the detector’s linearity and energy resolution by analyzing the total energy *deposited* in the calorimeter across varying incident energies. This phase involves calibrating the simulated detector response and examining the relationship between incident energy and measured energy deposition.

#### 3.2.1. Energy Deposition and Calibration

To assess the energy resolution, the simulation tracks the total energy deposited in the calorimeter from each of the 1000 events. The total energy deposition is calculated as the integral of the charged particle density along the entire crystal length, effectively summing the energy lost via ionization. Photons are excluded from this analysis to focus solely on electron-positron contributions.

*Initial Calibration*—An initial simulation with 1 GeV incident electrons is used to *calibrate* the detector. When particles of fixed energy incident energy  $E_0$  strike the lead calorimeter, the measured energies from each particle form a Gaussian distribution in energy centered at  $E_0$ . The standard deviation then defines the *energy* resolution of the detector. Hence, using the initial 1 GeV simulation, the measured mean of the resultant energy deposition Gaussian distribution is measured and can afterwards be *scaled* accordingly to yield a distribution with a mean of 1GeV, thereby calibrating the detector. The measured energy resolution normal distribution is shown in Figure 3.

Therefore, to calibrate the detector, the total energy deposition for each event was scaled down by 3x, aligning the mean deposition with the known incident energy. This 3x calibration was consistently effective across multiple incident energies, yielding histogram means within  $\pm 0.03\text{GeV}$  of the expected values. The 3x increase in pre-calibrated simulated energy deposits likely stems from not acknowledging energy conservation and defining ionization loss to be directly proportional to distance

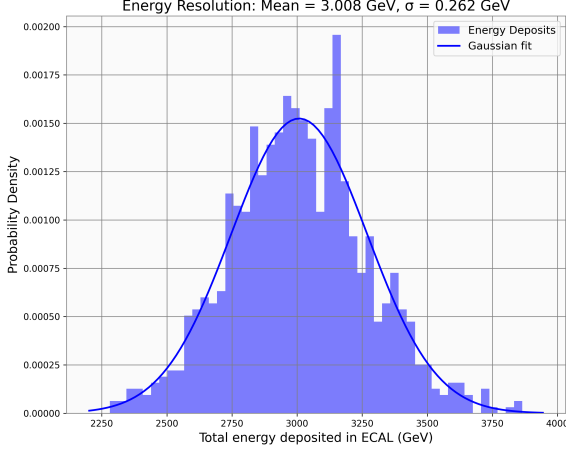


**Figure 3.** Energy deposition distribution results for a 1000 electrons of 1 GeV incident energy. The resultant mean was measured to be 3.008 GeV with a standard deviation of 0.262 GeV, hinting the detector should be scaled down by 3x for calibration.

travelled in the calorimeter, without limiting it to the incident particle's energy.

### 3.2.2. Simulation at Multiple Incident Energies

Now that the Monte Carlo simulation is calibrated, it was run for incident energies of 1, 3, 5, and 10 GeV. For each incident energy, the average charged particle count as a function of calorimeter depth was measured and is plotted similarly to Figure 1 in Figure 4.

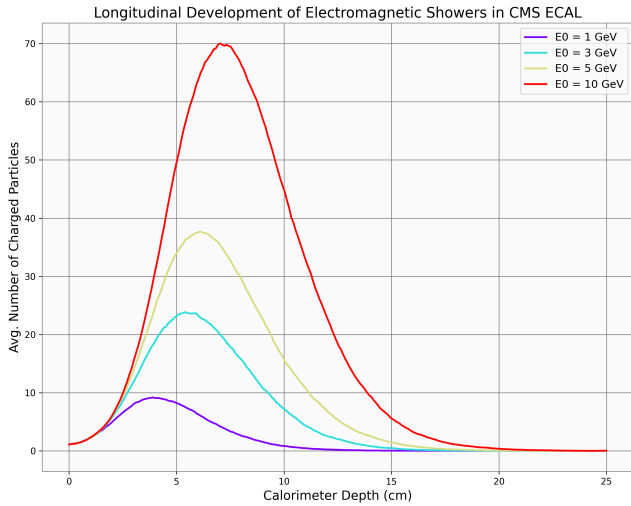


**Figure 4.** Average number of charged particles as a function of calorimeter depth for incident energies of 1, 3, 5, and 10 GeV. Higher incident energies result in increased average charged particle densities and shifts further in the shower maximum depth.

*Results*—As the incident energy increases, the average number of charged particles in the shower increases linearly, while the depth at which the peak number of charged particles occurs shifts deeper into the calorimeter. Specifically, the peak occurs 4.01cm at 1 GeV incident energy and extends to 7.25cm for 10 GeV incident energy, corresponding to 4.5 and 8.15 radiation lengths respectively. The longitudinal distributions maintain a Gaussian distribution shape, with higher energies resulting in steeper distributions.

The relationship between average energy deposited in the calorimeter and the incident energy was plotted below in Figure 5, revealing a perfect linear relationship described by a slope of 1.00.

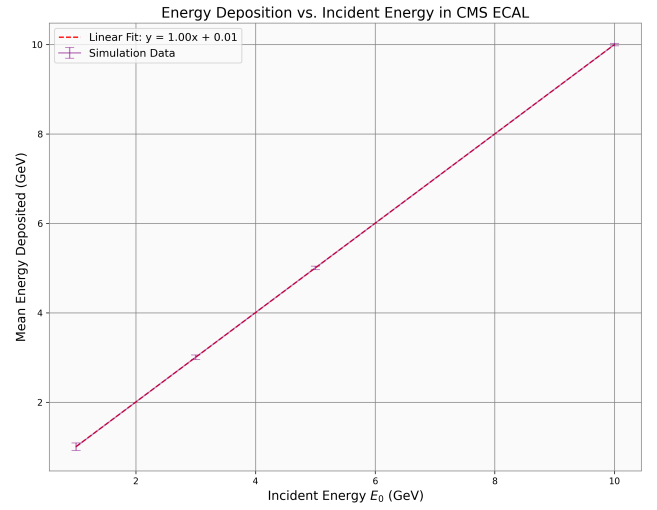


**Figure 5.** Average energy deposition in the calorimeter as a function of incident energy. The relationship is perfectly linear, with a calibration factor of 1.00 and an intercept of 0.01, indicating accurate detector calibration under simplifying assumptions.

This linearity is a direct consequence of the simplifying assumptions made in the simulation, particularly the proportionality of ionization energy loss to distance traveled and the equal energy sharing in the bremsstrahlung processes.

### 3.3. Energy Resolution Scaling

The energy resolution of the calorimeter is proportional to the standard deviation of the total energy deposition of an electromagnetic shower as shown in Figure 3 by the equation. To determine how the resolution of the calorimeter scales with the incident energy, the standard deviation of the energy deposition distribution divided by the incident energy is plotted against 1, 3, 5, and 10 GeV incident energies like before.



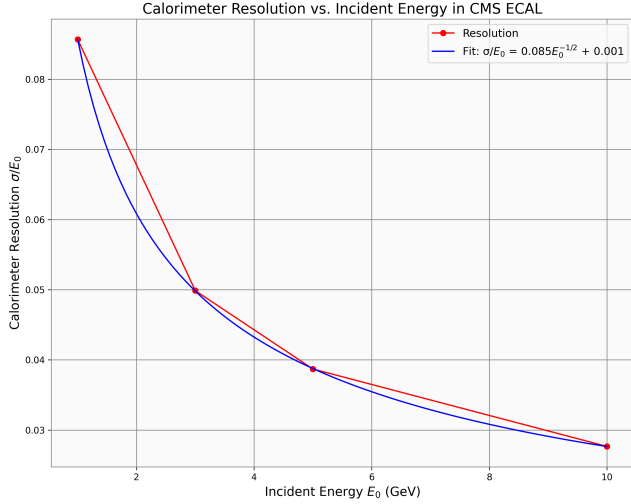


**Figure 6.** Calorimeter energy resolution ( $\sigma/E_0$ ) as a function of incident energy. The resolution follows an inverse square root dependence, fitting the relation  $\sigma/E_0 = 0.0851/\sqrt{E_0} + 0.001$ , where  $E_0$  is the incident energy.

The resolution follows an inverse square-root dependence, best described by the fit  $\sigma = 0.0851/\sqrt{E_0} + 0.001$ . This matches the *inverse* square-root dependence  $\sigma/E \propto 1/\sqrt{E}$  that is typically found in CMS reports (CMS Collaboration 2024).

#### 3.4. Phase 3: Fitting the Energy Deposition Function

Phase 3 involves fitting the energy deposition function to a gamma distribution to characterize the shower development. The energy deposition per unit length is modeled by the equation

$$\frac{dE}{dt} = E_0 b \frac{(bt)^{a-1} e^{-bt}}{\Gamma(a)}$$

where  $t$  is the dimensionless length scale  $x/X_0$ , with  $X_0$  being the radiation length, and  $a, b$  are constants to which the data is fit. Since the simulation tracks the number of charged particles rather than energy, the charged particle density is normalized by the total number of charged particles deposited at 1 GeV, effectively providing a conversion constant from the number of particles to energy in GeV.

Using the results from Phase 2, the parameters  $a$  and  $b$  were derived for incident energies of 1, 3, 5, and 10 GeV. The results are summarized in Table 1.

These parameters indicate how the energy deposition profile evolves with increasing incident energy, reflecting changes in the shower development dynamics within the calorimeter.

#### 3.5. Phase 4: Linearity and Resolution vs. Calorimeter Depth

$E_0$ (GeV)	$a$	$b$
1	0.7991	0.0030
3	0.8622	0.0032
5	0.8784	0.0031
10	0.9400	0.0037

**Table 1.** Energy resolution parameters at different incident energies.

Phase 4 examines how the performance of the calorimeter changes as a function of its thickness, measured in radiation lengths  $X_0$ . Specifically, it investigates the onset of non-linearities in the energy response and analyzes how energy resolution scales with calorimeter depth.

##### 3.5.1. Mean Energy Deposition vs. Incident Energy for Varying Depths

The simulation was run for calorimeter depths of 5, 10, 15, 20, and 25  $X_0$ , and the mean energy deposition was recorded for incident energies of 1, 3, 5, and 10 GeV shown in Figure 7.

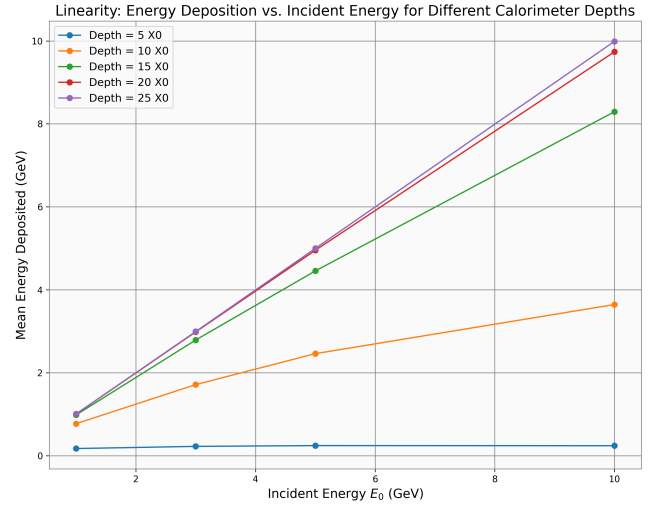


**Figure 7.** Mean Energy Deposition vs. Incident Energy  $E_0$  for calorimeter depths of 5, 10, 15, 20, and 25  $X_0$  showcasing how energy deposition approaches linearity with increasing calorimeter crystal depths.

At a calorimeter depth of  $5X_0$ , the mean energy deposited remained nearly constant, ranging from depositing 0.26 GeV at  $E_0 = 1$  GeV to depositing 0.26 GeV at  $E_0 = 10$  GeV. This is expected, as the calorimeter is not deep enough to absorb the incident particle and its products with the constant ionization energy loss used in the simulation. Hence the energy deposition is limited by the depth of the calorimeter, making it equivalent across all  $E_0$ . Increasing the depth to  $10X_0$ , the en-

ergy deposition follows a relatively linear trend with a slight decrease in slope between 5 and 10 GeV. This non-linearity likely stems from the shower maximum occurring before  $10X_0$  at 5 GeV, but occurring after  $10X_0$  at 10 GeV. There is a drastic change in the number of particles capable of being absorbed and depositing energy in the calorimeter between 5 and 10 GeV. Further increasing the crystal depth to 15, 20, and  $25X_0$  resulted in an increasingly linear trend, with exponentially diminishing differences in energy deposition as the calorimeter becomes deeper. This is expected as the calorimeter begins to exceed the maximum depth electrons of incident energy  $E_0$  can penetrate, thereby making the energy deposition at  $20X_0$  nearly identical to  $25X_0$ .

### 3.5.2. Linearity Ratio vs. Incident Energy for Varying Depths

The linearity ratio, defined as the mean energy deposition divided by the incident energy is plotted against the incident energies for various calorimeter depths in Figure 8

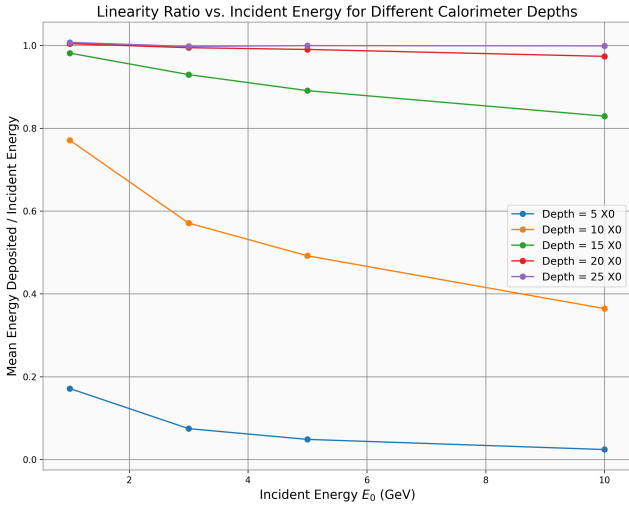


**Figure 8.** Linearity ratio (Mean Energy Deposited / Incident Energy) vs. Incident Energy for different calorimeter depths. Non-linearities emerge at smaller depths and stabilize at larger depths.

At a calorimeter depth of  $5X_0$ , the linearity ratio was approximately 0.183 at 1 GeV and decreased to 0.032 at 10 GeV, following the expected *inverse* square root trend, flattening with increased incident energy, that was not observed in Phase 2. At  $10X_0$ , the ratio was 0.779 at 1 GeV and decreased to 0.383 at 10 GeV, exhibiting a steeper trend. Deeper calorimeters (15, 20, and  $25X_0$ ) show reduced differences in linearity across incident energies with trends becoming more flat as calorimeter depth increases. This overall trend be-

tween the calorimeter depths is expected. At shallower depths like  $5X_0$ , electrons with higher incident energies are capable of depositing progressively smaller fractions of their initial energies before escaping the calorimeter. At larger depths like 20 and  $25X_0$ , all of the electron's incident energy is capable of being deposited; the electron being ultimately absorbed, resulting in a constant linearity ratio of 1.0 across all  $E_0$ .

### 3.5.3. Energy Resolution vs. Incident Energy for Varying Depths

Figure 9 illustrates the energy resolution  $\sigma/E_0$  as a function of incident energy for calorimeter depths 5, 10, 15, 20, and  $25X_0$ .

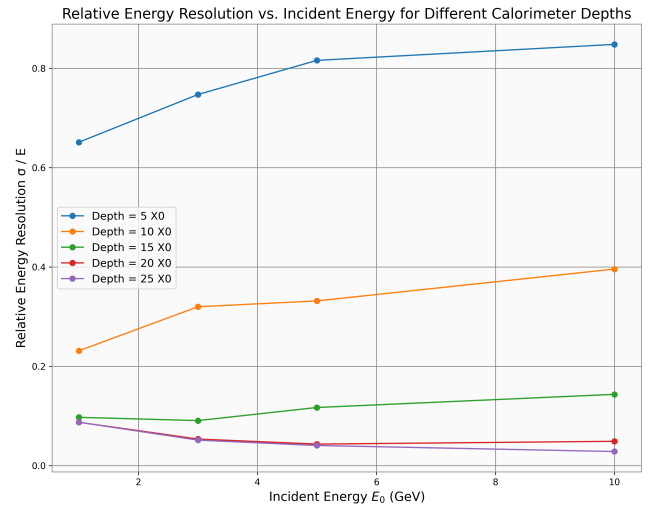


**Figure 9.** Energy Resolution ( $\sigma/E_0$ ) vs. Incident Energy for different calorimeter depths. The resolution follows an unexpected square root trend for smaller calorimeter depths, and follows the appropriate inverse-square root trend for larger depths.

At a calorimeter depth of  $5X_0$ , the energy resolution was highest, following an unexpected square-root trend caused by the calorimeter not absorbing all the energy of the incident electron(s). At a depth of  $10X_0$  the resolution becomes less of a square-root and starts “becoming” the proper inverse square-root function that is expected of calorimeter resolutions. At a depth of 20 and  $25X_0$ , with the calorimeters being able to fully absorb the incident electron(s), the resolution follows the appropriate inverse square-root relationship observed in the CMS ECAL calorimeter (CMS Collaboration 2024). Therefore, it seems as calorimeter depths increase, the energy resolution of the detector becomes increasingly “more inverse square-root”-like. Hence, for appropriate physical detectors that are used in real high-energy physics, a calorimeter of large depth, sufficient to fully

absorb incident particle(s) should be used to maximize detector energy resolution and readout.

#### 4. CONCLUSION

This study presents a Monte Carlo simulation of the one-dimensional longitudinal development of electromagnetic showers in the CMS electromagnetic calorimeter using a one-dimensional model.

**Phase 1** focused on simulating the shower profile for 1 GeV incident electrons in a 25 cm deep lead tungstate crystal, successfully replicating key features observed in established benchmarks (e.g. [CMS Collaboration \(2024\)](#), [Groom and Klein \(2019\)](#)). The peak charged particle density and its position within the calorimeter aligned with theoretical expectations, demonstrating the validity of the simulation approach despite the simplifying assumptions employed.

**Phase 2** extended the simulation to evaluate the detector's linearity and energy resolution across incident energies of 1, 3, 5, and 10 GeV. The calibration procedure effectively aligned the mean energy deposition with the known incident energies, and the results exhibited a perfect linear relationship between incident energy and measured energy deposition. Additionally, the energy resolution was found to scale with the inverse square-root of the incident energy, consistent with CMS reports ([CMS Collaboration 2024](#)).

**Phase 3** involved fitting the energy deposition function to a gamma distribution, extracting parameters  $a$  and  $b$  for various incident energies. The fitted parameters provide a quantitative characterization of the shower development and demonstrate how the energy deposition profile evolves with increasing energy.

**Phase 4** explored the detector's performance as a function of calorimeter thickness. The results indicated that thinner calorimeters ( $5X_0$ ) exhibit significant non-linearities in energy response and higher relative energy resolution. As the calorimeter depth increases to  $10X_0$  and beyond, the energy deposition approaches linearity, and the energy resolution improves, following expected scaling behaviors. These findings highlight the importance of calorimeter depth in optimizing detector performance and minimizing non-linearities in energy measurements.

The simulation's agreement with PDG benchmarks and CMS expectations underscores its potential as a foundational tool for further studies. Future work will involve incorporating more realistic physical processes, such as continuous bremsstrahlung energy loss and transverse shower spreading, as well as extending the simulation to three dimensions, higher incident energies, and different calorimeter materials. These en-

hancements aim to provide a more comprehensive understanding of the CMS ECAL's performance, contributing to more accurate energy measurements and improved particle identification in high-energy physics experiments.



## REFERENCES

- S. Agostinelli, J. Allison, K. Amako, J. Apostolakis, H. Araujo, P. Arce, M. Asai, D. Axen, S. Banerjee, G. Barrand, F. Behner, L. Bellagamba, J. Boudreau, L. Broglia, A. Brunengo, H. Burkhardt, S. Chauvie, J. Chuma, R. Chytrcek, G. Cooperman, and D. Zschesche. Geant4—a simulation toolkit. *Nuclear Instruments and Methods in Physics Research Section A: Accelerators, Spectrometers, Detectors and Associated Equipment*, 506(3):250–303, 2003. URL [https://doi.org/10.1016/S0168-9002\(03\)01368-8](https://doi.org/10.1016/S0168-9002(03)01368-8). URL [https://doi.org/10.1016/S0168-9002\(03\)01368-8](https://doi.org/10.1016/S0168-9002(03)01368-8).
- R. M. Brown. The cms electromagnetic calorimeter. *Nuclear Instruments and Methods in Physics Research Section A: Accelerators, Spectrometers, Detectors and Associated Equipment*, 572(1):29–32, 2007. URL <https://doi.org/10.1016/j.nima.2006.10.240>. URL <https://doi.org/10.1016/j.nima.2006.10.240>.
- CMS Collaboration. Performance of the cms electromagnetic calorimeter in pp collisions at  $\sqrt{s} = 13$  tev. 2024. URL <https://arxiv.org/abs/2403.15518v2>.
- N. Folkerts, J. Putzer, S. Villalba-Chávez, and C. Müller. Electron-positron pair creation in the superposition of two oscillating electric field pulses with largely different frequency, duration and relative positioning. *arXiv preprint arXiv:2303.02350*, 2023. URL <https://arxiv.org/abs/2303.02350>.
- D. E. Groom and S. R. Klein. Passage of particles through matter. August 2019. URL <https://pdg.lbl.gov/2019/reviews/rpp2018-rev-passage-particles-matter.pdf>. Revised.
- Particle Data Group and R. L. Workman. Review of particle physics. *Progress of Theoretical and Experimental Physics*, 2022(8):083C01, 2022. URL <https://doi.org/10.1093/ptep/ptac097>. URL <https://doi.org/10.1093/ptep/ptac097>.
- Polina Simkina, Fabrice Couderc, Julie Malclès, and Mehmet Özgür Sahin. Reconstruction of electromagnetic showers in calorimeters using deep learning. *arXiv preprint arXiv:2311.17914*, 2023. URL <https://arxiv.org/abs/2311.17914>.
- Jean-Charles Walter and Gerard Barkema. An introduction to monte carlo methods. *arXiv preprint arXiv:1404.0209*, 2014. URL <https://arxiv.org/abs/1404.0209>.